Simulation of ring-exchange models with projected entangled pair states

Chao Wang, Shaojun Dong, Yongjian Han,* and Lixin He†

CAS Key Laboratory of Quantum Information, University of Science and Technology of China, Hefei 230026, Anhui, China and Synergetic Innovation Center of Quantum Information and Quantum Physics, University of Science and Technology of China, Hefei, 230026, China

(Received 14 August 2021; revised 19 December 2021; accepted 3 January 2022; published 18 January 2022)

Algorithms to simulate ring-exchange models on a square lattice using projected entangled pair states (PEPSs) are developed. We generalize the imaginary time evolution (ITE) method to optimize PEPS wave functions for the models with ring-exchange interactions. We compare the effects of different approximations of the environment. To understand the numerical instability during optimization, we introduce the "singularity" of a PEPS and develop a regulation procedure that can effectively reduce the singularity of a PEPS. We benchmark our method with the toric code model and obtain extremely accurate ground-state energies and topological entanglement entropy. We also benchmark our method with the two-dimensional cyclic ring-exchange model, and find that the ground state has a strong vector chiral order. The algorithms can be a powerful tool to investigate the models with ring interactions. The methods developed in this work, e.g., the regularization process to reduce the singularity, can also be applied to other models.

DOI: 10.1103/PhysRevB.105.024417

I. INTRODUCTION

Recently, models with ring-exchange interactions have attracted growing attention. Ring-exchange interactions were first introduced as higher-order perturbation terms of the Hubbard model near half filling [1–10]. It has been shown that the ring-exchange interactions may play important roles in many materials [10–13]. The ring-exchange terms can stabilize the uncondensed boson liquid [14–18], which helps to reveal the physics of strange metal in the high-T_c superconductors [19]. The J-Q model, which includes the ring-exchange interactions, has been used [20,21] to demonstrate the deconfined quantum critical point [22]. The ring-exchange interactions are also crucial in the lattice-gauge models [23–25] to exhibit topological phase transitions. Recently, the ring-exchange interactions have been realized experimentally in the cold atom systems [26,27].

The ring-exchange models have been studied by various numerical methods, including the exact diagonalization (ED) [9,15,28,29], the quantum Monte Carlo (QMC) [30], and the density-matrix renormalization group (DMRG) [31] methods. However, these methods all have some limitations. For example, the ED method can only treat rather small systems, whereas the QMC may suffer from the sign problems in the fermionic and frustrated systems [21,32]. The DMRG method can only treat the quasi-one-dimensional systems [15,28,33].

The recent developed tensor network states (TNS) methods [34–38], including the projected entangled states (PEPS) method, are very promising to study the two-dimensional many-particle systems, which has been successfully applied to various models, such as the J_1-J_2 model [39], kagome Heisenberg model [40], and the t-J model [41,42]. The studies of the ring-exchange models via infinite PEPS (iPEPS) [43–45] have been performed by using the gradient optimization method [46–48]. However, the gradient optimization starting from a random finite PEPS may suffer from local minima.

The imaginary time evolution method (ITE) may be more efficient and may effectively avoid the local minima. The results of ITE can be used as the starting wave functions for further gradient optimization [46–48]. However, the ring-exchange models on a square lattice involve four-site interactions, which are significantly more complicated than the bond-interaction models for the PEPS. So far, no effective ITE algorithm has been developed for the general ring-exchange models [49] because of the complication of the four-site interactions. In this work, we develop an efficient ITE update algorithm to optimize the PEPS for the ring-exchange models. Combined with the stochastic gradient optimization methods [48], it provides a powerful tool to study the ring-exchange models.

This paper is organized as follows: In Sec. II, we introduce the algorithms to optimize the PEPS for the ring-exchange models. After introducing a general algorithm of ITE for the ring-exchange model, we discuss the approximations of the environment in Sec. II A. In Sec. II B we discuss how to control the "singularity" of the PEPS, to enhance the numerical stability during the ITE. In Sec. III, we benchmark the algorithms on the toric code model, in which we calculate the ground-state energies and the topological entanglement entropy of the model. In Sec. IV, we apply the algorithms to study the cyclic ring-exchange model. We summarize in Sec. V.

*smhan@ustc.edu.cn
†helx@ustc.edu.cn

II. METHOD

We consider a general Hamiltonian with ring-exchange interactions on the square lattices,

$$H = \sum_i H_{1,i} + \sum_{i,j} H_{2,i,j} + \sum_p H_{\square,p}, \tag{1}$$

where $H_{1,i}$, $H_{2,i,j}$ denote the one-site and two-site interaction terms, respectively. $H_{\square,p}$, which acts on plaquettes p, denotes the ring-exchange interaction terms.

We solve the ground state of the above Hamiltonian using the PEPS method [36]. A PEPS on an $L_1 \times L_2$ square lattice can be written as

$$|\Psi\rangle = \prod_{i=1,j=1}^{L_1,L_2} \left[T^{[i,j]}_{l_{ij}r_{ij}u_{ij}d_{ij}s_{ij}} \delta_{r_{ij}l_{i,j+1}} \delta_{d_{ij}u_{i+1,j}}\right] \bigotimes_{i=1,j=1}^{L_1,L_2} |s_{ij}\rangle, \tag{2}$$

where Einstein's sum rule is assumed. In this equation, $T^{[i,j]}_{l_{ij}r_{ij}u_{ij}d_{ij}s_{ij}}$ is a rank-five complex tensor at site (i, j) which has four auxiliary indices $l_{ij}, r_{ij}, u_{ij}, d_{ij}$ and a physical index s_{ij}. Each auxiliary index is summed from 1 to the bond dimension D, and each physical index is summed from 1 to the physical dimension d.

The ground state $|\Psi_{\rm GS}\rangle$ of Hamiltonian H in the form of PEPS can be optimized by using the ITE algorithm [50],

$$\begin{aligned} |\Psi_{\rm GS}\rangle &= \lim_{\tau\to\infty} e^{-H\tau}|\Psi_0\rangle \\ &= \lim_{N\to\infty} \left(\prod_{i=1}^{n} e^{-\Delta\tau H_i} \prod_{i=n}^{1} e^{-\Delta\tau H_i}\right)^N |\Psi_0\rangle, \end{aligned} \tag{3}$$

where $|\Psi_0\rangle$ is a randomly chosen initial PEPS. The ITE is divided into small time steps, i.e., $\Delta\tau \ll 1$, which can be well approximated by the products of a series of local operators H_i using the Trotter expansion [51].

The key ingredient of the ITE algorithm is to efficiently approximate the $(n+1)$th step wave function $|\Psi_{n+1}\rangle = e^{-\Delta\tau H_i}|\Psi_n\rangle$ by a PEPS, which we call a local update process. We regard the sites, where the operator $e^{-\Delta\tau H_i}$ acts on, as the system (which includes four sites on a plaquette for the ring-exchange interaction model), and the rest of the lattice as the environment. During the local update process, the environment tensors are fixed, while the system tensors are updated to obtain a best approximation of $\||\Psi_{n+1}\rangle - e^{-\Delta\tau H_i}|\Psi_n\rangle\|$. Generally we have to make some approximations to the environment to simplify the calculations. The quality of the approximated environment often plays a critical role in determining the system tensors during the ITE [52].

For the bond-interaction models, a simple update (SU) scheme has been developed [53] for the local update process, in which the environment tensor for each virtual bond of the system is assumed to be irrelevant and can be approximated by a real diagonal matrix. Generally, the SU scheme involves four steps, as illustrated in Fig. 1: (i) to absorb environment tensors into the system [Fig. 1(b)]; (ii) to contract the system tensors with the time evolution operator $e^{-\Delta\tau H_i}$ [Fig. 1(c)]; (iii) the contracted system tensor is approximated by a new PEPS [Fig. 1(d)]; and (iv) the environment tensors are split from the new system tensors [Fig. 1(d)].

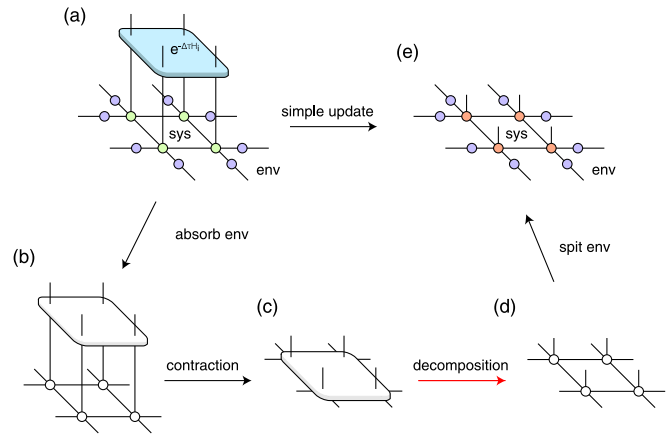

FIG. 1. Schematic illustration of a simple update method for the time evolution $|\Psi_{n+1}\rangle = e^{-\Delta\tau H_i}|\Psi_n\rangle$.

However, we cannot naively apply the SU to the ring-exchange models for two reasons: First, the third step in the above algorithm is the crucial part of the SU. For the bond-interaction models, which only involve two-site interactions, this can be done by singular value decomposition (SVD) [53] or higher-order singular value decomposition (HOSVD) [38]. However, for a ring-exchange interaction $H_{\square,i}$, there is no simple technique to decompose the tensor in Fig. 1(c) into a ring tensor network in Fig. 1(d). Second, the SU oversimplifies the environment, which causes serious accuracy and numerical stability problems for the ring-exchange models.

Therefore, we have to use an alternative way to perform the local update process by direct minimizing the error function [52,54],

$$\mathrm{Err}(|\Psi_{n+1}\rangle) = \||\Psi_{n+1}\rangle - e^{-\Delta\tau H_i}|\Psi_n\rangle\|, \tag{4}$$

where $|\Psi_{n+1}\rangle$ is the new PEPS to approximate the TNS after time-evolution $e^{-\Delta\tau H_i}$, and $\|\cdot\|$ is the two-norm of a state. The error function Err is a quadratic function for each tensor in the system, which can be minimized by iteratively solving the equation $\partial_{T^*}\mathrm{Err}(|\Psi_{n+1}\rangle) = 0$, i.e.,

$$T \cdot A_T = B_T, \tag{5}$$

where,

$$A_T = \partial_T \partial_{T^*} \langle\Psi_{n+1}|\Psi_{n+1}\rangle, \tag{6}$$

$$B_T = \partial_{T^*} \langle\Psi_{n+1}|e^{-\Delta\tau H_i}|\Psi_n\rangle, \tag{7}$$

for each tensor T of $|\Psi_{n+1}\rangle$ in the system part. The tensor networks that correspond to A_T, B_T are shown in Figs. 2(a)–2(b). In practice, we solved the equation for each tensor with other tensors kept fixed, and repeated the process for 20 sweeps.

A. Calculation of A_T and B_T: Approximation of the environment

To calculate tensor A_T and B_T, one has to contract the environment shown in Fig. 2(c). The environment tensor should be Hermitian and positive semidefinite to ensure the error functions in Eq. (4) bounded from below [52]. The exact contraction of the environment tensor networks certainly satisfies the conditions, which unfortunately cannot be done

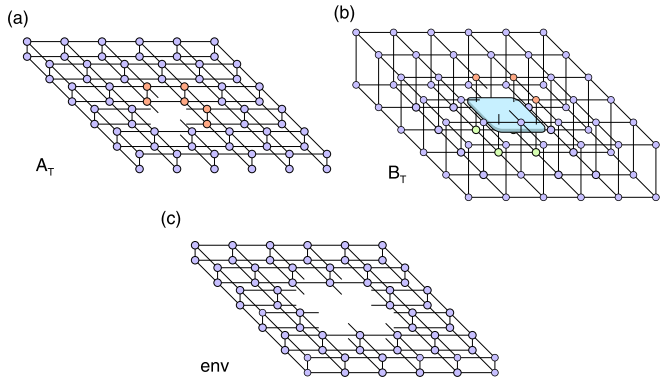

FIG. 2. The tensor networks of (a) A_T and (b) B_T for the system tensor T defined in Eqs. (6) and (7), respectively, and (c) the environment tensor networks for A_T and (b) B_T.

because the computational cost grows exponentially with the size of the networks. The approximations to the environment have been discussed comprehensively in Ref. [52] for bond-interaction models. Here, we discuss the approximation of the environment for the ring-exchange models.

1. Simple environment

If we neglect the entanglement between sites 1–8 connected to the system tensors in Fig. 3(a), the approximated the environment is just the direct products of Hermitian positive semidefinite matrices on each site in (bra and ket) pairs [see Fig. 3(c)]. This is the simplest approximation of the environment, known as the simple environment [53,55]. Obviously the simple environment is automatically Hermitian and positive semidefinite according to its structure.

For an open boundary system, we can obtain the simple environment as follows: We first approximate the tensors at the boundary by the direct products of Hermitian positive semidefinite tensors by setting $D_c = 1$ within the row. We then contract the boundary tensors to the next row, and again approximate the obtained row of tensors as direct products, as shown Fig. 3(b). We repeat this procedure until all environment tensors have been contracted, resulting in the simple environment shown in Fig. 3(c).

With the simple environment approximation, tensors A_T and B_T can be easily calculated. The time complexity to compute A_T and B_T and solve Eq. (5) is $O(D^6)$, compared with $O(D^5)$ for bond-interaction models, where D is the bond dimension of the PEPS. This computation cost is relatively low. The update scheme with the simple environment approximation is also called a generalized SU method in Ref. [55]. The (generalized) SU methods works quite well for many bond-interactions models, if the correlations in the PEPS are not very strong. For more complicated ring-exchange models, due to the over-simplification of the environment, the SU method can have poor accuracy, which will be discussed in Sec. IV.

2. Cluster environment

To improve the accuracy of the ITE, we need a better approximation to the environment than the simple environment.

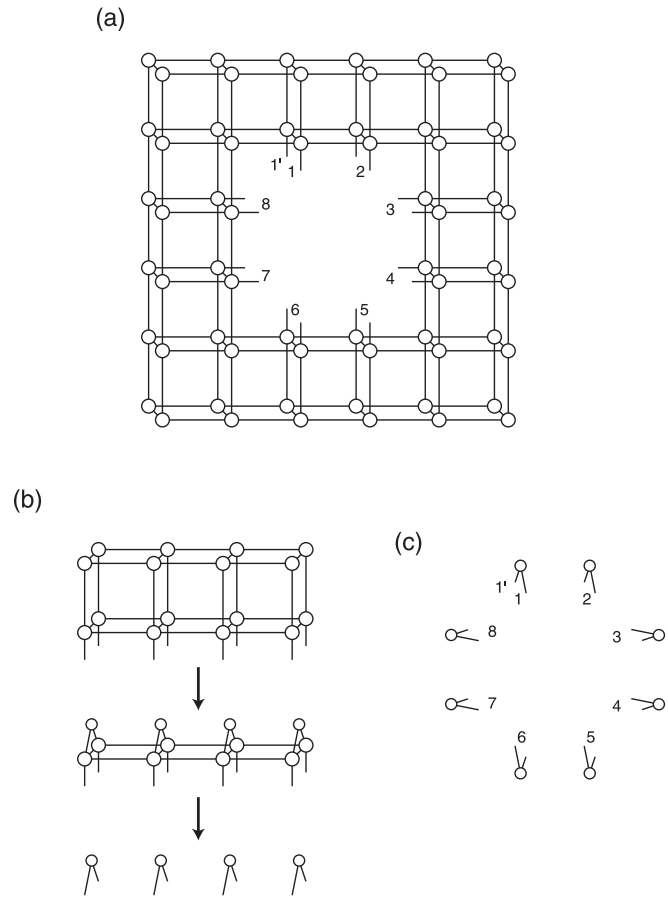

FIG. 3. (a) The exact environment of a 2×2 ring tensors in a square PEPS. (b) The simple environment approximation during contraction of environment. (c) The final simple environment as a product state of the tensors on the eight sites connected to the system.

One can directly contract the environment via the boundary-MPO (bMPO) methods [52,56]. However, if a truncation to the bond dimension, D_c is used, the obtained environment is not guaranteed to be positive semidefinite. One way to restore the positive semidefiniteness of the environment is to diagonalize the environment tensors and remove all negative eigenvalues [52]. This procedure works fine for bond-interaction models. However, for the ring-exchange model, the final environment tensor is a $D^8 \times D^8$ matrix, which is extremely expensive to diagonalize for large D.

Instead, we adopt the cluster environment approximation [55]. We contract the tensors via the boundary MPO method with $D_c = 1$, as in the simple environment approximation, except for the tensors which are directly connected with the systems tensors (see Fig. 4). To see that the cluster environment is positive semidefinite, we may decompose each simple environment tensor E, which is Hermitian and positive semidefinite by construction, into $QQ^\dagger$, as illustrated by Figs. 4(b) and 4(c). By doing so, the cluster environment becomes the contraction of a tensor network with its own conjugate, which is guaranteed to be Hermitian and positive semidefinite. With the cluster environment approximation, the time complexity to compute A_T and B_T and solve Eq. (5) is $O(D^{12})$, where D is the bond dimension of original PEPS

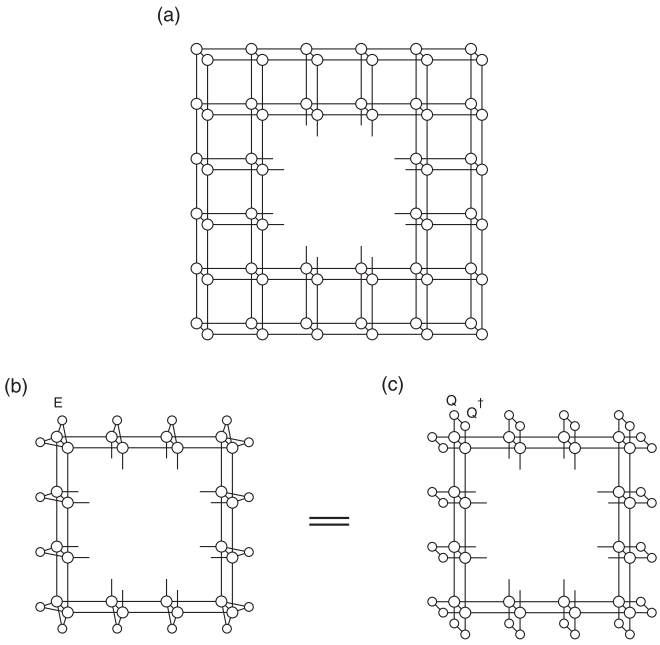

FIG. 4. (a) Exact environment of a 2×2 ring tensor in a square PEPS. (b) The cluster environment. (c) The equivalent cluster environment that is obviously Hermitian and positive semidefinite.

wave function, which is higher than the simple environment approximation. The time complexity is also higher than that of cluster update for bond interaction, which is $O(D^{10})$ [52].

B. Reduce the singularity of a projected entangled state

After we obtain the (simple or cluster) environment, we may apply time-evolution operators with ring-exchange terms. However, we find that, during the ITE, there is a strong numerical instability after some time steps. In previous works [52,56,57], this numerical instability was attributed to the unfixed gauge freedom of PEPS. Some gauge-fixing methods are proposed to avoid the problem. However the relation between the gauge freedom and the numerical instability remains unclear, and there was no standard to choose the best gauge.

To understand the numerical instability during ITE, we define the "singularity" of a PEPS, and we show that the numerical instability is due to the rapid growth of the "singularity" of the PEPS.

Let $|\Psi\rangle$ be the PEPS defined in Eq. (2), and the singularity of $|\Psi\rangle$ is defined as

$$\mathrm{sing}(|\Psi\rangle) = \frac{\prod_i \|T_i\|}{\langle\Psi|\Psi\rangle}, \tag{8}$$

where T_i is the ith tensor of the tensor network and $\|\cdot\|$ is the two-norm of a tensor. The singularity of Ψ characterize the reciprocal of the norm of $\langle\Psi|\Psi\rangle$, when each tensor T_i is normalized to $\|T_i\| = 1$. When the norm of a tensor network approaches zero, the singularity diverges. There are some special PEPS, e.g., PEPS in canonical form [58], and the isometric tensor network state [59] naturally has low singularity.

In practice, we find that the singularity of the tensor networks grows rapidly during the ITE if untreated, and the update process becomes numerically unstable [60]. To solve this issue, we note that a PEPS has some gauge freedom, e.g., one may insert a pair of invertible gauge matrices $I = GG^{-1}$ in each virtual bond, and the norm of $\langle\Psi|\Psi\rangle$ is invariant. However, by absorbing the G and G^{-1} matrices to the tensors, $\|T_i\|$ may change, and as a consequence the singularity of the PEPS may vary. Therefore, it is possible to reduce the singularity by choosing proper gauges of the PEPS.

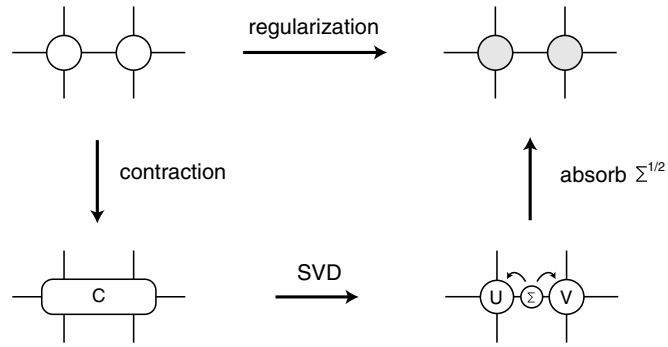

FIG. 5. The regularization procedure for a bond in the tensor network.

Here, we propose a regularization procedure to reduce the singularity of a PEPS. For each bond of the PEPS, we first contract the two tensors connected by the bond, resulting in a tensor C, and we then make a SVD, $C = U\Sigma V$. The tensors of the two sites are updated as $U\Sigma^{1/2}$ and $\Sigma^{1/2}V$, respectively. This process is illustrated in Fig. 5. As proved in Theorem 2 in the Appendix, these regularization operations minimize the singularity of the bond tensors, when all other tensors remain fixed. We sweep all the bonds in the PEPS with this procedure for a few iterations until the singularity of the tensor network converges.

To demonstrate the effectiveness of the method, we optimize the ground state of a cyclic ring-exchange model introduced in Sec. IV on a 4×4 square lattice. For convenience, the bond dimension of the PEPS is taken to be $D = 2$. We adopt the cluster environment approximation. During the ITE, we compared the energies and the singularities with and without the regularization process at each time step. The results are shown in Fig. 6. As we see, without the regularization procedure, the singularity of the PEPS grows very rapidly with time steps. As a consequence, after 340 steps, the evolution becomes numerically unstable. In contrast, with the

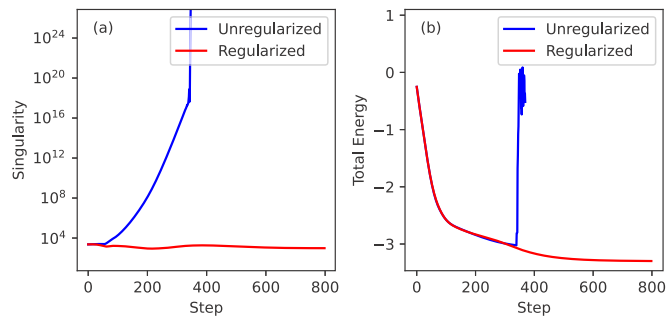

FIG. 6. (a) Singularities and (b) energies of the PEPS during the ITE optimization with and without regularization of the singularity.

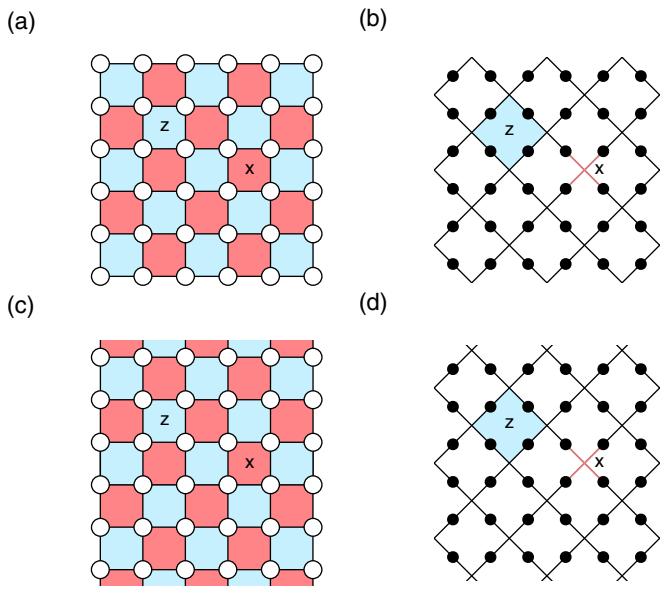

FIG. 7. (a) Toric-code model on a square lattice with OBC, where spins locate on vertices. P_z are the blue plaquettes and P_x are the red plaquettes. (b) The original Kitaev's toric code model, where spins locate on edges. (c), (d) The corresponding toric-code models with CBC.

regularization procedure, the singularity remains at low level during the ITE, and the energy can be steadily optimized.

C. Gradient optimization

Because of the drastic approximation to the environment (even for the cluster environment) during the ITE, the resulting ground state may not be accurate enough. It has been demonstrated that the gradient optimization after ITE can significantly improve the ground-state energies for the bond-interaction models, where the energy and the gradients are calculated via a Monte Carlo sampling technique with relative low time complexity [48,61,62]. These techniques can also be applied to the ring-exchange models in a similar manner. We perform the gradient optimization after the ITE, and we show in the following sections that, for some ring-exchange models, the gradient optimization can significantly improve the ground-state energies.

III. APPLICATION TO TORIC-CODE MODEL

We first apply our method to the toric-code model [25]. The toric-code model is a paradigm model with ring-exchange interactions that can be exactly solved on square lattices. Generally, the Hamiltonian of the toric code model is defined as

$$H = -\sum_{p\in P_x}\prod_{i\in p}\sigma_i^x - \sum_{p'\in P_z}\prod_{i\in p'}\sigma_i^z, \tag{9}$$

where P_x and P_z are alternative plaquettes of the lattice, as shown in Fig. 7, in which Figs. 7(a) and 7(c) correspond to the open boundary condition (OBC) and cylindrical boundary condition (CBC), respectively. We included the appropriate boundary terms such that our model is equivalent to Kitaev's original model with smooth boundary conditions, as shown in Figs. 7(b) and 7(d).

TABLE I. The exact ground energies of the toric-code model of various sizes with both OBC and CBC. The relative errors of the numerical results are less than 10^{-14}.

Boundary condition	System size	Theoretical energy	Relative simulation error
OBC	4×4	-17	$<10^{-14}$
	6×6	-37	
	8×8	-65	
	10×10	-101	
CBC	4×4	-16	
	6×6	-36	
	8×8	-64	
	10×10	-100	

The physical properties, e.g., the topological degeneracy, of the toric-code model are closely related to the boundary conditions. The ground state of the toric-code model with OBC is nondegenerate, and has twofold degeneracy on a cylinder [63]. More specifically, the ground state of the toric-code model on a cylinder has a gapped $\mathbb{Z}_2$ topological order, which has nontrivial low-energy excitations [25]. The topological entanglement entropy (TEE) in the ground-state manifold (GSM), which is used to character the topological order, is therefore $\ln 2$ on a cylinder [63].

It has been shown that the ground state of toric-code model can be exactly expressed by PEPS with bond dimension $D = 2$ [64]. Therefore toric-code model serves as a good benchmark for our method. In this section, we benchmark our method by calculating the ground-state wave functions of the toric-code model on square lattices and investigating its topological properties.

We first obtain the ground-state wave functions of the toric model using PEPS of bond dimension $D = 2$, on square lattices of various sizes. Both OBC and CBC are studied, with the smooth boundary conditions [65]. We use ITE with simple environment approximation to optimize the ground state, and the imaginary time step is set to $\Delta\tau = 0.02$. The ground-state energies converge very fast with the time steps. The exact ground-state energies and relative errors of our numerical results to the exact results of various lattice sizes are listed in Table I for both OBC and CBC. It is interesting to see that one can obtain the ground-state energies with nearly machine accuracy for the toric-code model using only a simple environment.

We then calculate the TEE [66] of the ground states of the toric-code model with CBC to characterize their topological order. We divide the cylinder into left ($\mathcal{L}$) and right ($\mathcal{R}$) parts, as shown in Fig. 8. Let $|s_\mathcal{R}\rangle$ be the basis of the Hilbert space of the part $\mathcal{R}$, the reduced density matrix of $|\Psi\rangle$ of part $\mathcal{L}$ is $\rho_\mathcal{L} = \sum_{s_\mathcal{R}}\langle s_\mathcal{R}|\Psi\rangle\langle\Psi|s_\mathcal{R}\rangle$. The αth order Rényi entropy of a state $|\Psi\rangle$ between the two parts is defined as

$$H_\alpha = \frac{1}{1-\alpha}\ln \mathrm{Tr}\left(\rho_\mathcal{L}^\alpha\right). \tag{10}$$

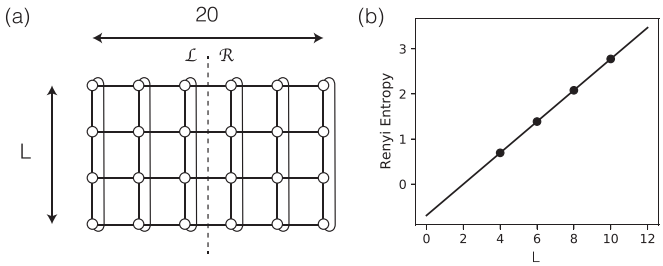

FIG. 8. (a) The $L \times 20$ cylindrical lattice, as well as the PEPS, are divided into $\mathcal{L}$, $\mathcal{R}$ parts. (b) Linear fit of H_2-L data for toric-code model with CBC, where the topological entanglement entropy is ln 2.003

Generally, the Rényi entropy is proportional to the size of the boundary (L) between the two parts, i.e., when $L \to \infty$, it has the form

$$H_\alpha = -\gamma + aL + \cdots, \tag{11}$$

where the ellipses represent terms that vanish in the limit of $L \to \infty$. The constant γ, which is independent of the size of the system, is the TEE [67]. Note that the Rényi entropy is ambiguous in a degenerate GSM, and the TEE should be calculated on its minimal entanglement state (MES) [63].

To obtain the TEE, we study toric-code model on the $L \times 20$ rectangular lattices with CBC, which is periodic in the first dimension. The lattices are divided into the $\mathcal{L}$ and $\mathcal{R}$ parts, both have the size of $L \times 10$ as shown in Fig. 8(a). We calculate the second-order Rényi entropy between the two parts of the ground states in the whole GSM. We then obtain the minimal Rényi entropy in the GSM. More details can be found in Appendix B.

The numerically calculated Rényi entropies of the MES are listed in Table II, for $L = 4$–10, which are in excellent agreement with exact results. The Rényi entropy shows excellent linearity with L, as shown in Fig. 8(b), and the fitted TEE for the toric-code model with CBC is ln 2.003, which is in excellent agreement the theoretical result ln 2.

IV. APPLICATION TO CYCLIC RING-EXCHANGE MODEL

In this section, we investigate the ground state of the cyclic ring-exchange model [2–10] using the PEPS method developed in this work. The cyclic ring-exchange model on a square lattice can be written as

$$H = \sum_{(ijkl)} \left[\left(S_i \cdot S_j + \frac{1}{4} \right) \left(S_k \cdot S_l + \frac{1}{4} \right) + \left(S_i \cdot S_l + \frac{1}{4} \right) \right.$$

TABLE II. The minimal Rényi entropy of the toric-code model on $L \times 20$ cylinders.

System size	Boundary length	Theoretical H_2 for MES	Simulation value of H_2 for MES
4×20	4	ln 2	$\ln(2 + 2.8 \times 10^{-11})$
6×20	6	ln 4	$\ln(4 - 1.5 \times 10^{-5})$
8×20	8	ln 8	$\ln(8 + 1.6 \times 10^{-5})$
10×20	10	ln 16	ln 16.032

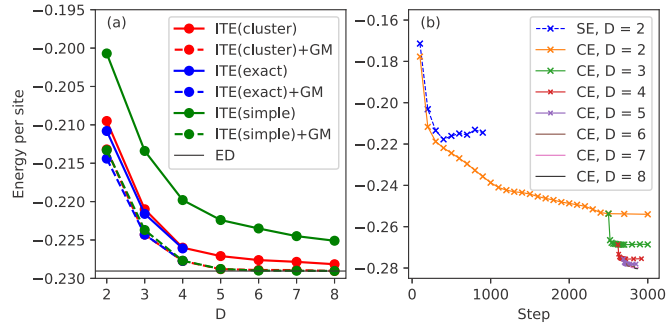

FIG. 9. (a) Comparing the ground-state energies of a cyclic ring-exchange model on the 4×4 lattice obtained by the simple environment and cluster environment (bond dimensions $D = 2$–8) to that by the exact environment ($D = 2$–4). The exact ground-state energy (ED) is also shown. (b) The ground-state energy of the cyclic ring-exchange model on the 10×10 lattice during ITE, with simple (SE) and cluster environment (CE). The bond dimensions are taken as $D = 2$–8.

$$\times \left(S_k \cdot S_j + \frac{1}{4} \right) - \left(S_i \cdot S_k - \frac{1}{4} \right) \left(S_j \cdot S_l - \frac{1}{4} \right) - \frac{1}{16} \Bigg]$$

$$= \sum_{(ijkl)} \left[\frac{1}{4} P_{ijkl} + \text{H.c.} - \frac{1}{16} \right], \tag{12}$$

where $(ijkl)$ denotes a 2×2 plaquette with four sites i, j, k, l in the clockwise order. Here, $i = (i_x, i_y)$ are the site index of the spin. The operator $P_{(ijkl)}$ performs a cyclic permutation of spins on i, j, k, l sites. The cyclic ring-exchange interactions arise naturally as higher-order terms in the magnetic effective model of half filled Hubbard model in the strong interaction limit [1], which plays an important role in many materials [10–13].

The cyclic ring-exchange model on a quasi-1D ladder lattice with width $L = 4$ has been investigated using the DMRG method [6]. The results indicate that the ground state of the model has a strong vector chiral order. Here we investigate the cyclic exchange model on the genuine two-dimensional (2D) lattices.

We calculate the ground states of the cyclic ring-exchange model on a $L \times L$ square lattice with $L = 4$–12 via PEPS. The maximum bond dimension $D = 8$ is used. During the calculations, we first perform ITE optimization imaginary time step $\Delta\tau = 0.02$ and until the energy (computed by MC sampling method [48]) is converged. We start from bond dimension $D = 2$, and gradually increase D. We use the optimized PEPS of D as the starting PEPS of $D + 1$.

In Fig. 9(a), we compare the energy after ITE on a 4×4 lattice with simple environment and cluster environment (bond dimensions $D = 2$–8), to those with exact environment ($D = 2$–4). As we see, for this system, the cluster environment works very well, which gives very accurate results compared with those with exact environment, whereas the energies of the simple environment are much higher after ITE. We note that, for this small system, starting from the PEPS obtained by ITE with simple environment, one can still obtain the correct ground-state energy by sufficiently long gradient optimization. In contrast, it takes much fewer gradient steps for the

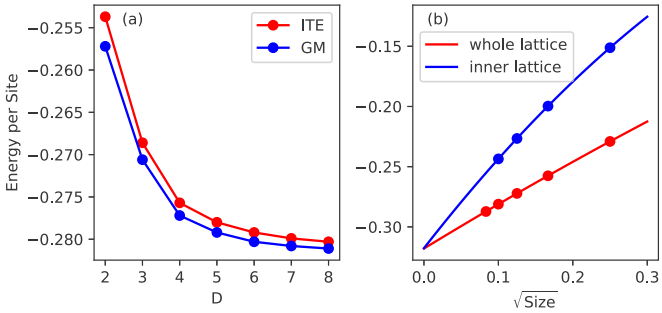

FIG. 10. (a) Comparing the ground-state energy of the cyclic ring-exchange model on the 10×10 lattice, obtained by the gradient optimization (GM) to ITE for bond dimensions $D = 2$–8. (b) The finite size scaling of the ground-state energies per site on the whole lattice and the inner sublattice, obtained by GM with bond dimension $D = 8$.

energy to converge, starting from the states obtained by cluster environment. Furthermore, one would expect that, for larger systems and more complicate models, ITE with simple environment followed by a gradient optimization method might fail converge to the correct ground state due to local minima.

The ground-state energies as functions of imaginary time steps on a 10×10 lattice are shown in Fig. 9(b) for different bond dimensions D. As a comparison, we also show the results obtained by simple environment for $D = 2$. We see that the energy can be optimized steadily using the cluster environment but not with the simple environment.

To obtain the highly accurate ground state, we further optimize the PEPS via the gradient optimization method [48] after ITE for each bond dimension D. In Fig. 10(a), we compare the ground-state energies of different bond dimensions obtained by the ITE to those by the gradient optimization method for the 10×10 lattice. We see that the gradient optimization can significantly improve the ground-state energy. For the 10×10 lattice, the ground-state energy of the model converges very well at $D = 8$.

The ground-state energies in the thermodynamic limit are calculated via finite-size scaling using the energies obtained by the gradient optimization for bond dimension $D = 8$. To see the boundary effects, we compare the energy per site calculated on the whole $L \times L$ lattice with that calculated on the $(L-2) \times (L-2)$ sublattice in the center region, and the results are shown in Fig. 10(b). The energy per site in the thermodynamic limit calculated on the whole lattice is $E_\infty = -0.3180$, determined by a second-order polynomial fitting, which agrees very well with $E_\infty = -0.3177$, calculated on the inner sublattice.

To determine the possible ordering in the ground state, we calculate spin-spin correlation function $S_{ij} = \langle S_i \cdot S_j \rangle - \langle S_i \rangle \cdot \langle S_j \rangle$, and dimer-dimer correlation function $D^\kappa_{ij} = \langle D^\kappa_i D^\kappa_j \rangle - \langle D^\kappa_i \rangle \langle D^\kappa_j \rangle$ $(\kappa = x/y)$ where $D^{x/y}_i = S_i \cdot S_{i+e_x/e_y}$. Their Fourier transformations,

$$S_{\mathbf{k}} = \frac{1}{L^4} \sum_{ij} e^{i\mathbf{k}\cdot(i-j)} S_{ij}, \tag{13}$$

$$D^\kappa_{\mathbf{k}} = \frac{1}{L^2(L-1)^2} \sum_{ij} e^{i\mathbf{k}\cdot(i-j)} D^\kappa_{ij}, \tag{14}$$

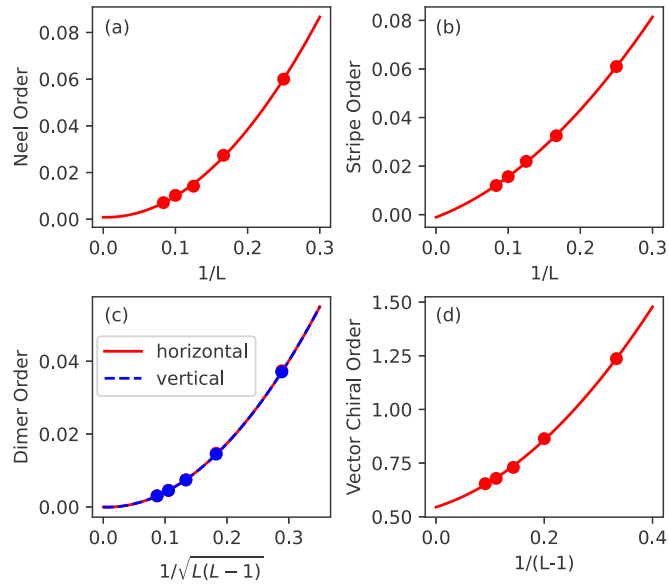

FIG. 11. Finite-size scaling of the (a) Néel order parameters $S_{(\pi,\pi)}$; (b) stripe order parameters $S_{(0,\pi)}$; (c) horizontal or vertical dimer order parameters $D^{x/y}_{(\pi,\pi)}$; (d) vector chiral order parameters $V_{(\pi,\pi)}$.

can be used as the order parameters. Especially $S_{(\pi,\pi)}$, $S_{(0,\pi)}$ are the order parameters of the Néel order and stripe order, respectively; whereas $D^\kappa_{(\pi,\pi)}$, $(\kappa = x, y)$ are the order parameters of the horizontal or vertical dimer orders.

Besides the Néel, stripe, and dimer order, a vector chiral phase that breaks space-inversion symmetry is also possible [6]. We also calculate the vector chiral-chiral correlation function,

$$V_{mn} = \langle V_m \cdot V_n \rangle - \langle V_m \rangle \cdot \langle V_n \rangle, \tag{15}$$

where $V_m = S_i \times S_j + S_j \times S_k + S_k \times S_l + S_l \times S_i$ is a vector operator on plaquette m, and i, j, k, l are four vertices of the plaquette in clockwise order. Its Fourier transformation,

$$V_{\mathbf{k}} = \frac{1}{(L-1)^4} \sum_{ij} e^{i\mathbf{k}\cdot(i-j)} V_{ij}, \tag{16}$$

at $\mathbf{k} = (\pi, \pi)$, is the order parameter of the vector chiral order.

The finite-size scaling of the order parameters are shown in Fig. 11. We find that the Néel order, stripe order, and dimer order all vanish in the thermodynamic limit $(L \to \infty)$, via second-order polynomial fitting. However, the vector chiral order parameter $V_{\pi,\pi} = 0.545$ remains large in the thermodynamic limit. These results suggest that the cyclic ring-exchange model has strong vector chiral order [6] in the two-dimensional lattice.

V. CONCLUSION AND OUTLOOK

We generalize the ITE to optimize PEPS wave functions for the ring-exchange models on two-dimensional lattices. We compare the effects of different approximations to the environment. We propose a scheme to reduce the singularity of the PEPS, which can significantly improve the numeric stability during the ITE. We benchmark our method with the toric-code

model and obtain extremely accurate ground-state energies and topological entanglement entropy. We also benchmark our method with the two-dimensional cyclic ring-exchange model and find that the ground state has a strong vector chiral order. This method can be a powerful tool to investigate the models with ring interactions, e.g., the Bose metal model [14–18] in genuine 2D systems. The methods developed in this work, e.g., the regularization process to reduce the singularity can also be applied to other models.

ACKNOWLEDGMENTS

We are grateful for the helpful discussion with C.-J. Wang. This work was supported by the National Science Foundation of China (Grants No. 11774327, and No.11874343). The numerical calculations have been done on the USTC HPC facilities.

APPENDIX A: SINGULARITY OF TENSOR NETWORK

Let TN be a tensor network (e.g., a PEPS) that consists of tensors $\{T_i\}$ such that the contraction of TN, contract(TN) $\neq 0$, the singularity of TN is defined as,

$$\text{sing(TN)} = \frac{\prod_i \|T_i\|}{\|\text{contract(TN)}\|}, \tag{A1}$$

where $\|\cdot\|$ stands for the two-norm of a tensor, unless otherwise noted. We say that the two tensor networks of the same structure (i.e., they have the same bond connections and bond dimensions) are equivalent if they give the same tensor after contraction. For a given TN [contract(TN) $\neq 0$], we would like to find the equivalent TN with minimal singularity, which we call the minimal singularity form of a TN.

Let $\mathcal{B}(A,B) =$ 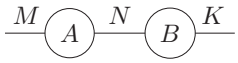 be a tensor network with bond dimensions M, N, K, respectively. We may treat A and B as matrices, and the contraction of the tensor network is just the matrix product AB. For this particularly simple kind of tensor networks, its minimal singularity form exists and can be rigorously obtained as follows:

Theorem 1. The minimal singularity form of $\mathcal{B}(A,B)$ exists.

Proof. We define the continuous function $\text{sing}_{\mathcal{B}}(A,B): \mathbb{C}^{M\times N}\times\mathbb{C}^{N\times K}\to\mathbb{R}$ by

$$\text{sing}_{\mathcal{B}}(A,B) = \text{sing}(\mathcal{B}(A,B)) = \frac{\|A\|\|B\|}{\|AB\|}. \tag{A2}$$

We need to prove that $\text{sing}_{\mathcal{B}}$ can reach its minimal value in the closed subset $S = \{(A',B')|A'B' = AB\}$.

According to Theorem 4.28 in Ref. [68], $\text{sing}_{\mathcal{B}}$ can reach its minimal value in the compact subspace $S' = \{(A',B')|\|A'\| \leqslant \|A\|,\ \|B'\| \leqslant \|B\|,\ A'B' = AB\}$. Let the minimum point be $(A_0,B_0)\in S'$. If (A_0,B_0) is not the minimum point in S, i.e., there exists $(A_1,B_1)\in S$, such that $\text{sing}_{\mathcal{B}}(A_1,B_1) < \text{sing}_{\mathcal{B}}(A_0,B_0)$, which implies that $\|A_1\|\|B_1\| < \|A_0\|\|B_0\|$. Therefore, we can always find a proper real number $\lambda > 0$, such that $(\lambda A_1, \frac{1}{\lambda}B_1)\in S'$, and $\text{sing}_{\mathcal{B}}(\lambda A_1, \frac{1}{\lambda}B_1) = \text{sing}_{\mathcal{B}}(A_1,B_1) < \text{sing}_{\mathcal{B}}(A_0,B_0)$. This contradicts the fact that (A_0,B_0) is the minimum point in S'. Therefore, (A_0,B_0) must be the minimum point in S. ■

Lemma 1. Let A be a complex matrix of shape $M\times N$. Let $A^\dagger A = W^\dagger \Sigma W$ be a diagonalization. By appropriate permutation, we can always ensure that $\Sigma = \text{diag}(\lambda_1,\ldots,\lambda_n,0,\ldots)$, where $\lambda_i > 0$. Then we have $A = V_A\Sigma_A W$ for some unitary V_A, where $\Sigma_A = \text{diag}(\sqrt{\lambda}_1,\ldots,\sqrt{\lambda}_n,0,\ldots)$ is a diagonal matrix of shape $M\times N$.

Proof. Similar to the proof of Theorem 11.4 in Ref. [69].■

Theorem 2. $\mathcal{B}(A_0,B_0)$, where $A_0B_0 = AB$, is the minimal singularity form of $\mathcal{B}(A,B)$ if and only if

$$A_0^\dagger A_0/\|A_0\|^2 = B_0B_0^\dagger/\|B_0\|^2. \tag{A3}$$

Proof. We first prove that Eq. (A3) is the necessary condition. Suppose that $\mathcal{B}(A_0,B_0)$ has minimal singularity. For an arbitrary infinitesimal matrix δS, let $A' = A_0e^{\delta S}$ and $B' = e^{-\delta S}B_0$, and the singularity of the tensor network $\mathcal{B}(A',B')$ is not less than that of $\mathcal{B}(A_0,B_0)$, i.e.,

$$\begin{aligned}\|A'\|^2\|B'\|^2 =& \|A_0e^{\delta S}\|^2\|e^{-\delta S}B_0\|^2\\ =& \|A_0(1+\delta S)\|^2\|(1-\delta S)B_0\|^2 + O(\delta S^2)\\ =& \|A_0\|^2\|B_0\|^2 + 2\text{Re}[\text{Tr}[(A_0^\dagger A_0\|B_0\|^2 -\\ & B_0B_0^\dagger\|A_0\|^2)\delta S]] + O(\delta S^2)\\ \geqslant& \|A_0\|^2\|B_0\|^2.\end{aligned} \tag{A4}$$

For the above inequality to hold for any δS, we must have

$$A_0^\dagger A_0\|B_0\|^2 - B_0B_0^\dagger\|A_0\|^2 = 0. \tag{A5}$$

It thus proves that Eq. (A3) is a necessary condition for Theorem 2.

Next, we prove Eq. (A3) is the sufficient condition for Theorem 2. Let A_0 and B_0 satisfy Eq. (A3), then we have,

$$\left(\frac{A_0}{\|A_0\|}\right)^\dagger\frac{A_0}{\|A_0\|} = \frac{B_0}{\|B_0\|}\left(\frac{B_0}{\|B_0\|}\right)^\dagger. \tag{A6}$$

By Lemma 1, we have,

$$\frac{A_0}{\|A_0\|} = V_{A_0}\Sigma_{A_0}W, \tag{A7}$$

$$\left(\frac{B_0}{\|B_0\|}\right)^\dagger = V_{B_0}\Sigma_{B_0}W, \tag{A8}$$

where Σ_{A_0} and Σ_{B_0} have identical nonzero diagonal elements, which are arranged before zero diagonal elements. Therefore,

$$A_0B_0 = V_{A_0}\Sigma_{A_0B_0}V_{B_0}^\dagger, \tag{A9}$$

where $\Sigma_{A_0B_0} = \|A_0\|\|B_0\|\Sigma_{A_0}\Sigma_{B_0}^T$.

Let $\Sigma_{A_0B_0} = \text{diag}(\lambda_1,\ldots,\lambda_n,0,\ldots)$ $(\lambda_i > 0)$. Since the right-hand side of Eq. (A9) is the SVD of matrix A_0B_0, $\{\lambda_i\}$ are the singular values A_0B_0. Therefore, $\sum\lambda_i$, which is also known as the nuclear norm $\|A_0B_0\|_*$, is completely determined by the matrix $A_0B_0 = AB$. Since $\|A_0\|\Sigma_{A_0}$ and $\|B_0\|\Sigma_{B_0}^T$ have proportional nonzero diagonal elements, we have

$$\|A_0\|\Sigma_{A_0} = m\text{diag}\left(\sqrt{\lambda}_1,\ldots,\sqrt{\lambda}_n,0,\ldots\right), \tag{A10}$$

$$\|B_0\|\Sigma_{B_0}^T = \frac{1}{m}\text{diag}\left(\sqrt{\lambda}_1,\ldots,\sqrt{\lambda}_n,0,\ldots\right), \tag{A11}$$

for some undetermined real number $m > 0$. The singularity of $\mathcal{B}(A_0, B_0)$ is then

$$\mathrm{sing}(\mathcal{B}(A_0, B_0)) = \frac{\|A_0\|\|B_0\|}{\|A_0 B_0\|} = \frac{\|AB\|_*}{\|AB\|}. \tag{A12}$$

Therefore, for any (A_0, B_0) that satisfies Eq. (A3), $\mathcal{B}(A_0, B_0)$ has the same singularity. Since we have proven that a minimal singularity form of $\mathcal{B}(A, B)$ must satisfy Eq. (A3), it thus proves that Eq. (A3) is also a sufficient condition for Theorem 2. ■

Particularly, A_0 and B_0 can be chosen as follows. Let $U\Sigma V$ be the SVD of the matrix AB, where Σ is a quasidiagonal singular matrix $\mathrm{diag}(\lambda_1, \ldots, \lambda_n, 0, \ldots)$ of shape $M \times K$, such that $\lambda_i > 0$. Let $\bar{\Sigma}_A$ be a quasidiagonal matrix $\mathrm{diag}(\sqrt{\lambda}_1, \ldots, \sqrt{\lambda}_n, 0, \ldots)$ of shape $M \times N$, and $\bar{\Sigma}_B$ be a quasidiagonal matrix $\mathrm{diag}(\sqrt{\lambda}_1, \ldots, \sqrt{\lambda}_n, 0, \ldots)$ of shape $N \times K$. It is easy to check that $A_0 = U\bar{\Sigma}_A$ and $B_0 = \bar{\Sigma}_B V$ is a solution to Eq. (A3). Therefore, $\mathcal{B}(U\bar{\Sigma}_A, \bar{\Sigma}_B V)$ is a minimal singularity form of $\mathcal{B}(A, B)$.

For a general tensor network, such as a PEPS, the existence of a minimal singularity form can be proved in a similar manner. However, we lack an efficient algorithm to find the exact minimal singularity form. Therefore, we may adopt an iteration update method to obtain a tensor network whose singularity is minimal against perturbation on any bond, by performing bond regulation and sweeping all bonds, as explained in Sec. II B. We have shown that this procedure can dramatically reduce the singularity of the tensor network, and allow steadily optimize the energy via ITE.

APPENDIX B: CALCULATION OF RÉNYI ENTROPY

In this Appendix we introduce the methods to calculate the Rényi entropy of a tensor network state [70].

Let $|\Psi\rangle$ be the ground state of a quantum system. If we divide the system into two parts denoted by $\mathcal{L}$ and $\mathcal{R}$, the state can be written by

$$|\Psi\rangle = \sum_{s_\mathcal{L} s_\mathcal{R}} \Psi_{s_\mathcal{L} s_\mathcal{R}} |s_\mathcal{L}\rangle |s_\mathcal{R}\rangle, \tag{B1}$$

where $s_\mathcal{L}$ and $s_\mathcal{R}$ are physical indices of $\mathcal{L}$ and $\mathcal{R}$ parts, respectively. The reduced density matrix with respect to part $\mathcal{L}$ is

$$\rho_\mathcal{L} = \mathrm{Tr}_\mathcal{R}(|\Psi\rangle\langle\Psi|) = \sum_{s_\mathcal{L} s'_\mathcal{L} s_\mathcal{R}} \Psi_{s_\mathcal{L} s_\mathcal{R}} \Psi^*_{s'_\mathcal{L} s_\mathcal{R}} |s_\mathcal{L}\rangle\langle s'_\mathcal{L}|, \tag{B2}$$

i.e., $(\rho_\mathcal{L})_{s_\mathcal{L} s'_\mathcal{L}} = \sum_{s_\mathcal{R}} \Psi_{s_\mathcal{L} s_\mathcal{R}} \Psi^*_{s'_\mathcal{L} s_\mathcal{R}}$. For simplicity, we write Eq. (B2) as $\rho_\mathcal{L} = \Psi \times \Psi^\dagger$.

The ground state of the system can be written as

$$\Psi_{s_\mathcal{L} s_\mathcal{R}} = \sum_{b_{\mathrm{aux}}} (\Psi_\mathcal{L})_{s_\mathcal{L} b_{\mathrm{aux}}} (\Psi_\mathcal{R})_{b_{\mathrm{aux}} s_\mathcal{R}}, \tag{B3}$$

where $\Psi_\mathcal{L}$ and $\Psi_\mathcal{R}$ are the subtensor networks of part $\mathcal{L}$ and $\mathcal{R}$, respectively, and b_{aux} are the auxiliary bonds that link the two subtensor networks. In the matrix form,

$$\Psi = \Psi_\mathcal{L} \times \Psi_R. \tag{B4}$$

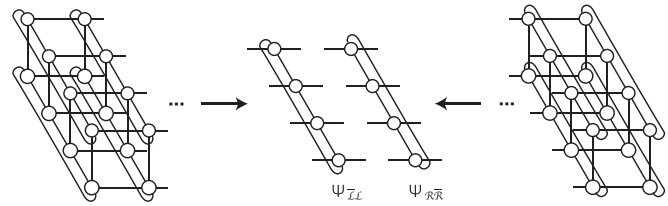

FIG. 12. Schematic illustrations of $\Psi_{\bar{\mathcal{L}}\mathcal{L}}$ and $\Psi_{\mathcal{R}\bar{\mathcal{R}}}$.

Then the trace of the αth power of the reduced density matrix can be obtained by

$$\begin{aligned}\mathrm{Tr}\left(\rho_\mathcal{L}^\alpha\right) &= \mathrm{Tr}((\Psi \times \Psi^\dagger)^\alpha) \\ &= \mathrm{Tr}((\Psi_\mathcal{L} \times \Psi_\mathcal{R} \times \Psi_\mathcal{R}^\dagger \times \Psi_\mathcal{L}^\dagger)^\alpha) \\ &= \mathrm{Tr}((\Psi_\mathcal{L}^\dagger \times \Psi_\mathcal{L} \times \Psi_\mathcal{R} \times \Psi_\mathcal{R}^\dagger)^\alpha).\end{aligned} \tag{B5}$$

For simplicity of the notation, we define $\Psi_{\bar{\mathcal{L}}\mathcal{L}} = \Psi_\mathcal{L}^\dagger \times \Psi_\mathcal{L}$ and $\Psi_{\mathcal{R}\bar{\mathcal{R}}} = \Psi_\mathcal{R} \times \Psi_\mathcal{R}^\dagger$, where $(\Psi_{\bar{\mathcal{L}}\mathcal{L}})_{b'_{\mathrm{aux}} b_{\mathrm{aux}}} = \sum_{s_\mathcal{L}} (\Psi_\mathcal{L})^*_{s_\mathcal{L} b'_{\mathrm{aux}}} (\Psi_\mathcal{L})_{s_\mathcal{L} b_{\mathrm{aux}}}$ and $(\Psi_{\mathcal{R}\bar{\mathcal{R}}})_{b_{\mathrm{aux}} b'_{\mathrm{aux}}} = \sum_{s_\mathcal{R}} (\Psi_\mathcal{R})_{b_{\mathrm{aux}} s_\mathcal{R}} (\Psi_\mathcal{R})^*_{b'_{\mathrm{aux}} s_\mathcal{R}}$. We may calculate $\Psi_{\bar{\mathcal{L}}\mathcal{L}}$ and $\Psi_{\mathcal{R}\bar{\mathcal{R}}}$ [52] as illustrated in Fig. 12, and $\mathrm{Tr}(\rho_\mathcal{L}^\alpha) = \mathrm{Tr}[(\Psi_{\bar{\mathcal{L}}\mathcal{L}} \times \Psi_{\mathcal{R}\bar{\mathcal{R}}})^\alpha]$, can be calculated by contracting the tensor network shown in Fig. 13. The αth Rényi entropy of between $\mathcal{L}$ and $\mathcal{R}$ parts of the system can be calculated by using Eq. (10). Here, we only calculate the second-order Rényi entropy (i.e., $\alpha = 2$).

If the GSM of the system are n-fold degenerate, we first obtain n linearly independent ground states $|\Psi_1\rangle, \ldots, |\Psi_n\rangle$ by independent simulations. We then perform the Gram-Schmidt orthogonalization process to obtain the orthonormalized states of the GSM, $|e_1\rangle, \ldots, |e_n\rangle$, where $|e_i\rangle = \sum_j v_{ij} |\Psi_j\rangle$. The Rényi entropy of MES is obtained by finding the minimal value of Rényi entropy of $|\Psi(\mathbf{c})\rangle = \sum_i c_i |e_i\rangle$ in the parameter space of $\mathbf{c}$.

Let $|\Psi(\mathbf{c})\rangle = \sum_i c_i |e_i\rangle = \sum_{i=1}^n \bar{c}_i |\Psi_i\rangle$, where $\bar{c}_i = \sum_j c_j v_{ji}$, be an arbitrary ground state. It is easy to show

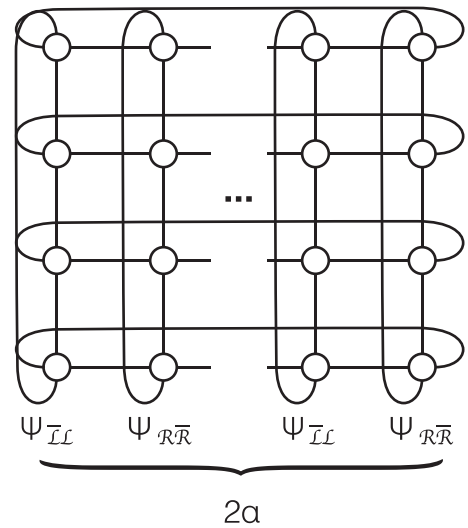

FIG. 13. Contracting the tensor network $(\Psi_{\bar{\mathcal{L}}\mathcal{L}} \times \Psi_{\mathcal{R}\bar{\mathcal{R}}})^\alpha$ gives $\mathrm{Tr}(\rho_\mathcal{L}^\alpha)$.

that

$$\mathrm{Tr}(\rho^2_{\Psi(\mathbf{c})}) = \mathrm{Tr}(\Psi(\mathbf{c}) \times \Psi^\dagger(\mathbf{c}) \times \Psi(\mathbf{c}) \times \Psi^\dagger(\mathbf{c})) = \sum_{ijkl} \bar{c}_i \bar{c}_j^\dagger \bar{c}_k \bar{c}_l^\dagger H_{ijkl}, \tag{B6}$$

where $H_{ijkl} = \mathrm{Tr}(\Psi_i \times \Psi_j^\dagger \times \Psi_k \times \Psi_l^\dagger)$, which can be calculated using the method discussed in the previous paragraphs.

Making use of the symmetry $H_{ijkl} = H_{klij}$ and $H_{ijkl} = H^*_{lkji}$, the number of independent H_{ijkl} can be reduced from n^4 to $\frac{1}{4}n^4 + \frac{3}{4}n^2$. With these H_{ijkl} calculated, one can obtain $\mathrm{Tr}(\rho^2_{\Psi(\mathbf{c})})$, and thus the second-order Rényi entropy using Eq. (B6).

For the toric-code model with CBC, the ground states are twofold degenerate. Any ground state can be parametrized by $|\Psi(\theta,\phi)\rangle = \cos\theta|e_1\rangle + e^{i\phi}\sin\theta|e_2\rangle$. Using the above method, the Rényi entropies H_2 in the (θ,ϕ) plane for different cylinder widths are calculated and shown in Figs. 14(a)–14(d), where the state with minimal H_2 in each figure corresponds to the MES.

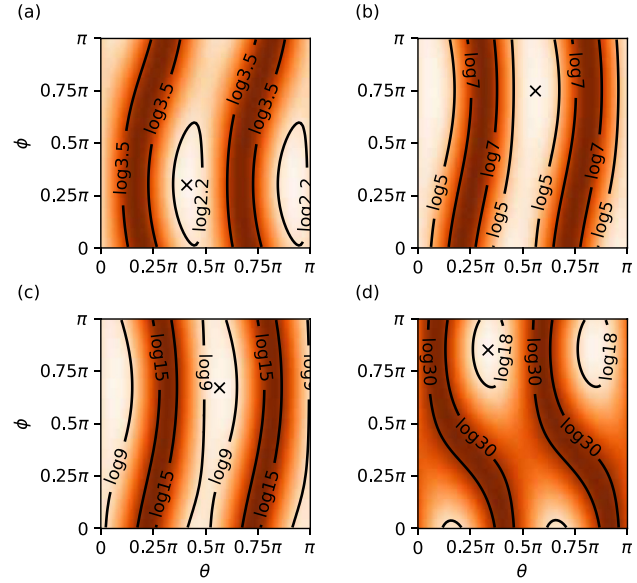

FIG. 14. The second-order Rényi entropy H_2 of the toric-code model with CBC, in GSM. The MES points are marked by "×." The results are obtained on the (a) 4×20, (b) 6×20, (c) 8×20, and (d) 10×20 lattices.

[1] A. H. MacDonald, S. M. Girvin, and D. Yoshioka, $\frac{t}{U}$ expansion for the Hubbard model, Phys. Rev. B **37**, 9753 (1988).

[2] A. Chubukov, E. Gagliano, and C. Balseiro, Phase diagram of the frustrated spin-1/2 Heisenberg antiferromagnet with cyclic-exchange interaction, Phys. Rev. B **45**, 7889 (1992).

[3] A. K. Kolezhuk and H.-J. Mikeska, Finitely correlated generalized spin ladders, Int. J. Mod. Phys. B **12**, 2325 (1998).

[4] S. Brehmer, H.-J. Mikeska, M. Müller, N. Nagaosa, and S. Uchida, Effects of biquadratic exchange on the spectrum of elementary excitations in spin ladders, Phys. Rev. B **60**, 329 (1999).

[5] M. Müller, T. Vekua, and H.-J. Mikeska, Perturbation theories for the $s = \frac{1}{2}$ spin ladder with a four-spin ring exchange, Phys. Rev. B **66**, 134423 (2002).

[6] A. Läuchli, G. Schmid, and M. Troyer, Phase diagram of a spin ladder with cyclic four-spin exchange, Phys. Rev. B **67**, 100409(R) (2003).

[7] V. Gritsev, B. Normand, and D. Baeriswyl, Phase diagram of the Heisenberg spin ladder with ring exchange, Phys. Rev. B **69**, 094431 (2004).

[8] J. Y. P. Delannoy, M. J. P. Gingras, P. C. W. Holdsworth, and A.-M. S. Tremblay, Néel order, ring exchange, and charge fluctuations in the half-filled Hubbard model, Phys. Rev. B **72**, 115114 (2005).

[9] J.-L. Song, S.-J. Gu, and H.-Q. Lin, Quantum entanglement in the $s = 1/2$ spin ladder with ring exchange, Phys. Rev. B **74**, 155119 (2006).

[10] J.-Y. P. Delannoy, A. G. Del Maestro, M. J. P. Gingras, and P. C. W. Holdsworth, Site dilution in the half-filled one-band Hubbard model: Ring exchange, charge fluctuations, and application to $La_2Cu_{1-x}(Mg/Zn)_xO_4$, Phys. Rev. B **79**, 224414 (2009).

[11] A. A. Katanin and A. P. Kampf, Spin excitations in La_2CuO_4: Consistent description by inclusion of ring exchange, Phys. Rev. B **66**, 100403(R) (2002).

[12] C. J. Calzado, C. de Graaf, E. Bordas, R. Caballol, and J.-P. Malrieu, Four-spin cyclic exchange in spin ladder cuprates, Phys. Rev. B **67**, 132409 (2003).

[13] A. M. Toader, J. P. Goff, M. Roger, N. Shannon, J. R. Stewart, and M. Enderle, Spin Correlations in the Paramagnetic Phase and Ring Exchange in La_2CuO_4, Phys. Rev. Lett. **94**, 197202 (2005).

[14] O. I. Motrunich and M. P. A. Fisher, d-wave correlated critical Bose liquids in two dimensions, Phys. Rev. B **75**, 235116 (2007).

[15] D. N. Sheng, O. I. Motrunich, S. Trebst, E. Gull, and M. P. A. Fisher, Strong-coupling phases of frustrated bosons on a two-leg ladder with ring exchange, Phys. Rev. B **78**, 054520 (2008).

[16] M. S. Block, R. V. Mishmash, R. K. Kaul, D. N. Sheng, O. I. Motrunich, and M. P. A. Fisher, Exotic Gapless Mott Insulators of Bosons on Multileg Ladders, Phys. Rev. Lett. **106**, 046402 (2011).

[17] R. V. Mishmash, M. S. Block, R. K. Kaul, D. N. Sheng, O. I. Motrunich, and M. P. A. Fisher, Bose metals and insulators on multileg ladders with ring exchange, Phys. Rev. B **84**, 245127 (2011).

[18] D. Huerga, J. Dukelsky, N. Laflorencie, and G. Ortiz, Chiral phases of two-dimensional hard-core bosons with frustrated ring exchange, Phys. Rev. B **89**, 094401 (2014).

[19] V. M. Galitski, G. Refael, M. P. A. Fisher, and T. Senthil, Vortices and Quasiparticles Near the Superconductor-Insulator Transition in Thin Films, Phys. Rev. Lett. **95**, 077002 (2005).

[20] A. W. Sandvik, Evidence for Deconfined Quantum Criticality in a Two-Dimensional Heisenberg Model with Four-Spin Interactions, Phys. Rev. Lett. **98**, 227202 (2007).

[21] A. W. Sandvik, Continuous Quantum Phase Transition between an Antiferromagnet and a Valence-Bond Solid in Two Dimensions: Evidence for Logarithmic Corrections to Scaling, Phys. Rev. Lett. **104**, 177201 (2010).

[22] T. Senthil, A. Vishwanath, L. Balents, S. Sachdev, and M. P. A. Fisher, Deconfined quantum critical points, Science **303**, 1490 (2004).

[23] T. Senthil and M. P. A. Fisher, Z_2 gauge theory of electron fractionalization in strongly correlated systems, Phys. Rev. B **62**, 7850 (2000).

[24] R. Moessner, S. L. Sondhi, and E. Fradkin, Short-ranged resonating valence bond physics, quantum dimer models, and Ising gauge theories, Phys. Rev. B **65**, 024504 (2001).

[25] A. Kitaev, Fault-tolerant quantum computation by anyons, Ann. Phys. (NY) **303**, 2 (2003).

[26] H.-N. Dai, B. Yang, A. Reingruber, H. Sun, X.-F. Xu, Y.-A. Chen, Z.-S. Yuan, and J.-W. Pan, Four-body ring-exchange interactions and anyonic statistics within a minimal toric-code Hamiltonian, Nat. Phys. **13**, 1195 (2017).

[27] A. Bohrdt, A. Omran, E. Demler, S. Gazit, and F. Grusdt, Multiparticle Interactions for Ultracold Atoms in Optical Tweezers: Cyclic Ring-Exchange Terms, Phys. Rev. Lett. **124**, 073601 (2020).

[28] G. Roux, S. R. White, S. Capponi, A. Läuchli, and D. Poilblanc, Doped two-leg ladder with ring exchange: Exact diagonalization and density matrix renormalization group computations, Phys. Rev. B **72**, 014523 (2005).

[29] C. B. Larsen, A. T. Rømer, S. Janas, F. Treue, B. Mønsted, N. E. Shaik, H. M. Rønnow, and K. Lefmann, Exact diagonalization study of the Hubbard-parametrized four-spin ring exchange model on a square lattice, Phys. Rev. B **99**, 054432 (2019).

[30] H. G. Evertz, The loop algorithm, Adv. Phys. **52**, 1 (2003).

[31] S. R. White, Density Matrix Formulation for Quantum Renormalization Groups, Phys. Rev. Lett. **69**, 2863 (1992).

[32] P. Henelius and A. W. Sandvik, Sign problem in Monte Carlo simulations of frustrated quantum spin systems, Phys. Rev. B **62**, 1102 (2000).

[33] F. B. Ramos and J. C. Xavier, n-leg spin-s Heisenberg ladders: A density-matrix renormalization group study, Phys. Rev. B **89**, 094424 (2014).

[34] R. Orus, A practical introduction to tensor networks: Matrix product states and projected entangled pair states, Ann. Phys. (NY) **349**, 117 (2014).

[35] G. Vidal, Efficient Classical Simulation of Slightly Entangled Quantum Computations, Phys. Rev. Lett. **91**, 147902 (2003).

[36] F. Verstraete and J. Cirac, Renormalization algorithms for quantum-many body systems in two and higher dimensions, arXiv:cond-mat/0407066.

[37] G. Vidal, Class of Quantum Many-Body States That Can Be Efficiently Simulated, Phys. Rev. Lett. **101**, 110501 (2008).

[38] Z. Y. Xie, J. Chen, J. F. Yu, X. Kong, B. Normand, and T. Xiang, Tensor Renormalization of Quantum Many-Body Systems Using Projected Entangled Simplex States, Phys. Rev. X **4**, 011025 (2014).

[39] W.-Y. Liu, S. Dong, C. Wang, Y. Han, H. An, G.-C. Guo, and L. He, Gapless spin liquid ground state of the spin-$\frac{1}{2}$ $J_1 - J_2$ Heisenberg model on square lattices, Phys. Rev. B **98**, 241109(R) (2018).

[40] H. J. Liao, Z. Y. Xie, J. Chen, Z. Y. Liu, H. D. Xie, R. Z. Huang, B. Normand, and T. Xiang, Gapless Spin-Liquid Ground State in the $s = 1/2$ Kagome Antiferromagnet, Phys. Rev. Lett. **118**, 137202 (2017).

[41] P. Corboz, T. M. Rice, and M. Troyer, Competing States in the t-j Model: Uniform d-Wave State Versus Stripe State, Phys. Rev. Lett. **113**, 046402 (2014).

[42] S.-J. Dong, C. Wang, Y.-J. Han, C. Yang, and L. He, Stable diagonal stripes in the t-j model at $\bar{n}h = 1/8$ doping from fPEPS calculations, npj Quantum Mater. **5**, 28 (2020).

[43] D. Poilblanc, Investigation of the chiral antiferromagnetic Heisenberg model using projected entangled pair states, Phys. Rev. B **96**, 121118(R) (2017).

[44] J.-Y. Chen, L. Vanderstraeten, S. Capponi, and D. Poilblanc, Non-Abelian chiral spin liquid in a quantum antiferromagnet revealed by an iPEPS study, Phys. Rev. B **98**, 184409 (2018).

[45] S. P. G. Crone and P. Corboz, Detecting a Z_2 topologically ordered phase from unbiased infinite projected entangled-pair state simulations, Phys. Rev. B **101**, 115143 (2020).

[46] L. Vanderstraeten, J. Haegeman, P. Corboz, and F. Verstraete, Gradient methods for variational optimization of projected entangled-pair states, Phys. Rev. B **94**, 155123 (2016).

[47] P. Corboz, Variational optimization with infinite projected entangled-pair states, Phys. Rev. B **94**, 035133 (2016).

[48] W.-Y. Liu, S.-J. Dong, Y.-J. Han, G.-C. Guo, and L. He, Gradient optimization of finite projected entangled pair states, Phys. Rev. B **95**, 195154 (2017).

[49] For some types of plaquette interaction terms, the four-site ITE evolution operator can be converted to a series of bond evolution operators [71].

[50] G. Vidal, Efficient Simulation of One-Dimensional Quantum Many-Body Systems, Phys. Rev. Lett. **93**, 040502 (2004).

[51] N. Hatano and M. Suzuki, Finding exponential product formulas of higher orders, in *Quantum Annealing and Other Optimization Methods* (Springer, Berlin, Heidelberg, 2005), pp. 37–68.

[52] M. Lubasch, J. I. Cirac, and M.-C. Bañuls, Algorithms for finite projected entangled pair states, Phys. Rev. B **90**, 064425 (2014).

[53] H. C. Jiang, Z. Y. Weng, and T. Xiang, Accurate Determination of Tensor Network State of Quantum Lattice Models in Two Dimensions, Phys. Rev. Lett. **101**, 090603 (2008).

[54] R. Haghshenas, S.-S. Gong, and D. N. Sheng, Single-layer tensor network study of the Heisenberg model with chiral interactions on a kagome lattice, Phys. Rev. B **99**, 174423 (2019).

[55] M. Lubasch, J. I. Cirac, and M.-C. Banuls, Unifying projected entangled pair state contractions, New J. Phys. **16**, 033014 (2014).

[56] H. N. Phien, J. A. Bengua, H. D. Tuan, P. Corboz, and R. Orús, Infinite projected entangled pair states algorithm improved: Fast full update and gauge fixing, Phys. Rev. B **92**, 035142 (2015).

[57] H. N. Phien, I. P. McCulloch, and G. Vidal, Fast convergence of imaginary time evolution tensor network algorithms by recycling the environment, Phys. Rev. B **91**, 115137 (2015).

[58] R. Haghshenas, M. J. O'Rourke, and G. K.-L. Chan, Conversion of projected entangled pair states into a canonical form, Phys. Rev. B **100**, 054404 (2019).

[59] M. P. Zaletel and F. Pollmann, Isometric Tensor Network States in Two Dimensions, Phys. Rev. Lett. **124**, 037201 (2020).

[60] Y. Zhang and E. Solomonik, On stability of tensor networks and canonical forms, arXiv:2001.01191.

[61] L. He, H. An, C. Yang, F. Wang, J. Chen, C. Wang, W. Liang, S. Dong, Q. Sun, W. Han, W. Liu, Y. Han, and W. Yao, PEPS++:

Towards extreme-scale simulations of strongly correlated quantum many-particle models on Sunway TaihuLight, IEEE Trans. Parallel Distrib. Syst. **29**, 2838 (2018).

[62] S.-J. Dong, C. Wang, Y. Han, G.-c. Guo, and L. He, Gradient optimization of fermionic projected entangled pair states on directed lattices, Phys. Rev. B **99**, 195153 (2019).

[63] Y. Zhang, T. Grover, A. Turner, M. Oshikawa, and A. Vishwanath, Quasiparticle statistics and braiding from ground-state entanglement, Phys. Rev. B **85**, 235151 (2012).

[64] C. Fernández-González, N. Schuch, M. M. Wolf, J. I. Cirac, and D. Pérez-García, Gapless Hamiltonians for the Toric Code Using the Projected Entangled Pair State Formalism, Phys. Rev. Lett. **109**, 260401 (2012).

[65] S. B. Bravyi and A. Y. Kitaev, Quantum codes on a lattice with boundary, arXiv:quant-ph/9811052.

[66] A. Kitaev and J. Preskill, Topological Entanglement Entropy, Phys. Rev. Lett. **96**, 110404 (2006).

[67] S. T. Flammia, A. Hamma, T. L. Hughes, and X.-G. Wen, Topological Entanglement Rényi Entropy and Reduced Density Matrix Structure, Phys. Rev. Lett. **103**, 261601 (2009).

[68] T. Apostol, *Mathematical Analysis: A Modern Approach to Advanced Calculus*, 2nd ed. (Pearson, 1974).

[69] D. Serre, *Matrices: Theory and Applications*, 2nd ed. (Springer, New York, 2010).

[70] J. I. Cirac, D. Poilblanc, N. Schuch, and F. Verstraete, Entanglement spectrum and boundary theories with projected entangled-pair states, Phys. Rev. B **83**, 245134 (2011).

[71] D. Robaina, M. C. Bañuls, and J. I. Cirac, Simulating $2+1DZ_3$ Lattice Gauge Theory with an Infinite Projected Entangled-Pair State, Phys. Rev. Lett. **126**, 050401 (2021).